Theses and Dissertations   1. Thesis and Dissertation Collection, all items

2006-06

Three-dimensional analysis of Azimuthal dependence of sound propagation through shallow-water internal solitary waves

Roush, Douglas L.

Monterey, California. Naval Postgraduate School

http://hdl.handle.net/10945/2798

NAVAL POSTGRADUATE SCHOOL

MONTEREY, CALIFORNIA

THESIS

THREE-DIMENSIONAL ANALYSIS OF AZIMUTHAL DEPENDENCE OF SOUND PROPAGATION THROUGH SHALLOW-WATER INTERNAL SOLITARY WAVES

by

Douglas L. Roush

June 2006

Thesis Advisor: John A. Colosi
Second Reader: D. Benjamin Reeder

Approved for public release; distribution is unlimited

THIS PAGE INTENTIONALLY LEFT BLANK

REPORT DOCUMENTATION PAGE		*Form Approved OMB No. 0704-0188*
Public reporting burden for this collection of information is estimated to average 1 hour per response, including the time for reviewing instruction, searching existing data sources, gathering and maintaining the data needed, and completing and reviewing the collection of information. Send comments regarding this burden estimate or any other aspect of this collection of information, including suggestions for reducing this burden, to Washington headquarters Services, Directorate for Information Operations and Reports, 1215 Jefferson Davis Highway, Suite 1204, Arlington, VA 22202-4302, and to the Office of Management and Budget, Paperwork Reduction Project (0704-0188) Washington DC 20503.		
1. AGENCY USE ONLY *(Leave blank)*	**2. REPORT DATE** June 2006	**3. REPORT TYPE AND DATES COVERED** Master's Thesis
4. TITLE AND SUBTITLE Three-Dimensional Analysis of Azimuthal Dependence of Sound Propagation through Shallow-Water Internal Solitary Waves		**5. FUNDING NUMBERS**
6. AUTHOR(S) Douglas L. Roush		
7. PERFORMING ORGANIZATION NAME(S) AND ADDRESS(ES) Naval Postgraduate School Monterey, CA 93943-5000		**8. PERFORMING ORGANIZATION REPORT NUMBER**
9. SPONSORING /MONITORING AGENCY NAME(S) AND ADDRESS(ES) N/A		**10. SPONSORING/MONITORING AGENCY REPORT NUMBER**
11. SUPPLEMENTARY NOTES The views expressed in this thesis are those of the author and do not reflect the official policy or position of the Department of Defense or the U.S. Government.		
12a. DISTRIBUTION / AVAILABILITY STATEMENT Approved for public release; distribution is unlimited		**12b. DISTRIBUTION CODE**

13. ABSTRACT (maximum 200 words)

     Results from shallow-water observational studies have shown acoustic field fluctuations in excess of 10 dB due primarily to non-linear internal solitary waves (ISWs). This work concentrates on three limitations ISWs pose to shallow-water acoustic propagation: anisotropy, quasi-deterministic-stochastic nature, and frequency dependence. These aspects are explored for low frequencies of 75 and 150 Hz through the development of a full-wave three-dimensional parabolic equation model in which a single ISW is introduced and rotated to achieve differing geometries between the ISW and acoustic transmission path. Two acoustic scattering regimes were found to exist: A horizontal refractive regime that generates very intense acoustic energy focusing and shadow zones near the ISW at range when the acoustic transmission path is nearly parallel to the ISW crest, and a vertical mode coupling regime producing moderate to strong acoustic energy focusing and shadow zones for all geometries. These three-dimensional patterns are similar for each frequency, but more intense for 150 Hz. The results dramatically show ISWs focus acoustic energy, dependent upon frequency and geometry, which may be exploitable in both a sonar performance and ambient noise modeling sense.

14. SUBJECT TERMS Internal Solitary Wave, Soliton, Shallow-Water Acoustic Propagation, Volume Scattering, Mode Coupling, Parabolic Equation Model		**15. NUMBER OF PAGES** 62
		16. PRICE CODE

17. SECURITY CLASSIFICATION OF REPORT Unclassified	**18. SECURITY CLASSIFICATION OF THIS PAGE** Unclassified	**19. SECURITY CLASSIFICATION OF ABSTRACT** Unclassified	**20. LIMITATION OF ABSTRACT** UL

NSN 7540-01-280-5500

Standard Form 298 (Rev. 2-89)
Prescribed by ANSI Std. 239-18

THIS PAGE INTENTIONALLY LEFT BLANK

THREE-DIMENSIONAL ANALYSIS OF AZIMUTHAL DEPENDENCE OF SOUND PROPAGATION THROUGH SHALLOW-WATER INTERNAL SOLITARY WAVES

Douglas L. Roush
Lieutenant, United States Navy
B.S., The University of Oklahoma, 1997

Submitted in partial fulfillment of the
requirements for the degree of

MASTER OF SCIENCE IN METEOROLOGY AND PHYSICAL OCEANOGRAPHY

from the

**NAVAL POSTGRADUATE SCHOOL
June 2006**

Author: Douglas L. Roush

Approved by: John A. Colosi
                 Thesis Advisor

                 D. Benjamin Reeder
                 Second Reader

                 Mary L. Batteen, Chair
                 Department of Oceanography

iii

THIS PAGE INTENTIONALLY LEFT BLANK

ABSTRACT

Results from shallow-water observational studies have shown acoustic field fluctuations in excess of 10 dB due primarily to non-linear internal solitary waves (ISWs). This work concentrates on three limitations ISWs pose to shallow-water acoustic propagation: anisotropy, quasi-deterministic-stochastic nature, and frequency dependence. These aspects are explored for low frequencies of 75 and 150 Hz through the development of a full-wave three-dimensional parabolic equation model in which a single ISW is introduced and rotated to achieve differing geometries between the ISW and acoustic transmission path. Two acoustic scattering regimes were found to exist: A horizontal refractive regime that generates very intense acoustic energy focusing and shadow zones near the ISW at range when the acoustic transmission path is nearly parallel to the ISW crest, and a vertical mode coupling regime producing moderate to strong acoustic energy focusing and shadow zones for all geometries. These three-dimensional patterns are similar for each frequency, but more intense for 150 Hz. The results dramatically show ISWs focus acoustic energy, dependent upon frequency and geometry, which may be exploitable in both a sonar performance and ambient noise modeling sense.

THIS PAGE INTENTIONALLY LEFT BLANK

TABLE OF CONTENTS

THIS PAGE INTENTIONALLY LEFT BLANK

LIST OF FIGURES

LIST OF TABLES

THIS PAGE INTENTIONALLY LEFT BLANK

ACKNOWLEDGMENTS

THIS PAGE INTENTIONALLY LEFT BLANK

I.   INTRODUCTION

Results from observational studies such as the SWARM (shallow-water acoustics in a random medium) experiment in 1995 on the continental shelf region of the New Jersey coast, the New England Shelfbreak PRIMER from 1995 to 1997, and the Asian Seas International Acoustics Experiment (ASIAEX) of 2001 in the northern South China Sea have illustrated significant acoustic field fluctuations in shallow-water environments with peak-to-peak acoustic energy fluctuations of more than 10 dB. An analysis of mode coupling due to internal solitary waves (ISWs) and their effects on modal intensity was documented by Tielburger, Finette and Wolf (1997). Further work by Preisig and Duda (1997) suggested ISWs typically appear as propagating pulse-like depressions of the thermocline which cause time variations in acoustic intensity and phase attributable to acoustic normal mode coupling. The analyses of these observational studies demonstrate some of the difficulties in understanding shallow-water acoustic propagation and sonar performance prediction in the presence of nonlinear ISWs.

ISWs are widespread and prominent features produced in shallow-water regions by tidal currents advecting stratified water over local bathymetry, producing an internal wave at tidal frequency (an internal tide). The internal tide evolves non-linearly into one or more oscillations, appearing as a single ISW or a packet of ISWs. Many coastal regions regularly produce ISWs with amplitudes of 50 to 100 m (Jackson, 2004).

This thesis concentrates on three effects ISWs impose on shallow-water acoustic propagation; anisotropy, a quasi-deterministic-stochastic nature, and frequency dependence. ISWs impart anisotropy to a shallow-water environment in that they are locally planar propagating wave fronts containing strong horizontal sound speed gradients in the direction of ISW propagation. Thus acoustic propagation is a function of the ISW's angle relative to the acoustic transmission path, i.e., propagation paths along verses across ISWs differ dramatically. ISWs are generally deterministic, appearing nearly every tide cycle given the same season, tidal phase, and bathymetry. However, they are stochastic in that their position, amplitude, width, and number vary based on tidal phase and season. Thus the presence of ISW(s) demonstrates a quasi-deterministic-

stochastic shallow-water acoustic propagation environment. It is well known that shallow-water acoustic propagation is strongly frequency dependent owing to bottom attenuation and water column absorption. Due to the small scale of ISWs and the resonant interaction of acoustic fields (Young, 2006) with ISWs, there is additional strong frequency dependence to the scattering.

The general influences on shallow-water acoustic propagation derive from the scattering effects of the surface, bottom, and volume. This thesis provides insight to shallow-water acoustic propagation concerning ISW limitations by specifically addressing the dependence on volume scattering through development of a full-wave three-dimensional parabolic equation (3DPE) model. While volume scattering has been modeled with techniques such as uncoupled 3D normal modes, ray and $N \times 2D$ methods, it has not been treated with a full-wave 3D modeling approach.

The anisotropic aspect of ISWs is explored by observing the acoustic variability as a function of ISW orientation. A single ISW is introduced into the 3DPE model which is then rotated in the *xy*-plane, thereby realizing differing angles between the ISW and acoustic transmission path. The deterministic character of shallow-water acoustic propagation concerning ISWs is analyzed by examining the acoustic energy field patterns and energy flux. The stochastic character is not explored in this work, but can be studied by varying ISW parameters. Frequency dependence was investigated by using 75 and 150 Hz.

The results dramatically show that across-ISW propagation is characterized by moderate mode coupling and little out-of-plane scattering, or a weak three-dimensional effect, while along ISW propagation is characterized by both strong mode coupling and out-of-plane scattering, or a strong three-dimensional effect with clearly defined focusing/defocusing regions. The mode energy was found to fluctuate in excess of 3 dB from an environment free of ISWs. Also, angular deflection of acoustic energy on the order of 1-5$^\mathrm{o}$ was found to exist near the ISW at range. Further, the angular deflection and associated energy fluctuations increase with range.

The actual limitations caused by ISWs such as acoustic energy fluctuations of 10 dB and phase fluctuations hampering signal processing and detection can be mitigated.

ISWs shape the ambient noise field and focus energy. Gaining knowledge of these patterns can allow for detection above noise. If knowledge is gained of the phase fluctuation statistics, better algorithms could be developed to enhance detection proficiency. Hence, this work has implications for both active and passive sonar capabilities in addition to ambient noise modeling.

Chapter II describes the development of the 3DPE model. Chapter III discusses model simulations, data sets and output display methods. Model analysis is provided for acoustic transmission paths in strictly along- and across-ISW geometries in the first section of Chapter IV. The second section of Chapter IV describes the acoustic energy flux and resulting acoustic modification regimes. The last section of Chapter IV provides analysis of acoustic transmission paths for intermediate ISW geometries. Conclusions and recommendations are provided in Chapter V.

THIS PAGE INTENTIONALLY LEFT BLANK

II. DEVELOPMENT OF A THREE-DIMENSIONAL PARABOLIC EQUATION MODEL

A. THREE-DIMENSIONAL STANDARD PARABOLIC EQUATION

The standard parabolic equation introduced by R. H. Hardin and F. D. Tappert in the early 1970s is used to simulate acoustic propagation, the derivation of which closely follows that of Jensen, Kuperman, Porter, & Schmidt (1994). The derivation begins with the Helmholtz equation for a homogeneous density medium in Cartesian coordinates

$$\nabla^2 p + \frac{\omega^2}{c^2} p = 0, \tag{1}$$

where p is the wave function describing the acoustic pressure, ω the angular frequency and c the sound speed. It is assumed that the solution to Equation (1) takes the form

$$p(x, y, z) = \psi(x, y, z) e^{ik_0 x}, \tag{2}$$

where ψ is the complex wave amplitude and $k_0 = \omega/c_0$ a reference wavenumber.

Taking the first and second derivatives of the solution yields

$$p' = \psi' e^{ik_0 x} + ik_0 \psi e^{ik_0 x} \tag{3}$$

and

$$p'' = \psi'' e^{2ik_0 x} + 2ik_0 \psi' e^{ik_0 x} - ik_0^2 \psi e^{ik_0 x}. \tag{4}$$

Substituting Equations (3) and (4) into the Helmholtz equation yields

$$\frac{\partial^2 \psi}{\partial x^2} + \frac{\partial^2 \psi}{\partial y^2} + \frac{\partial^2 \psi}{\partial z^2} + 2ik_0 \psi' - k_0^2 \psi + \frac{\omega^2}{c^2} \psi = 0. \tag{5}$$

The wave is assumed to be slowly changing in x. Hence, the paraxial approximation expressed by

$$\frac{\partial^2 \psi}{\partial x^2} \ll 2ik_0 \psi \tag{6}$$

is then introduced to obtain the form

$$2ik_0 \frac{\partial \psi}{\partial x} + \frac{\partial^2 \psi}{\partial y^2} + \frac{\partial^2 \psi}{\partial z^2} - \left(k_0^2 - k^2\right)\psi = 0. \tag{7}$$

The term $k_0^2 - k^2$ can be manipulated by using the index of refraction

$$n = \frac{c_0}{c}, \tag{8}$$

where

$$\left(k_0^2 - k^2\right) = k_0^2 \left(1 - \frac{c_0^2}{c^2}\right) = -k_0^2 \left(n^2 - 1\right) \tag{9}$$

to yield the final form of the three-dimensional standard parabolic equation

$$2ik_0 \frac{\partial \psi}{\partial x} + \frac{\partial^2 \psi}{\partial y^2} + \frac{\partial^2 \psi}{\partial z^2} + k_0^2 \left(n^2 - 1\right)\psi = 0. \tag{10}$$

We reiterate here that the numerical modeling of this shallow-water problem treats the seabed as a fluid medium, thus neglecting density changes in depth.

B.   MODELING METHOD

Range independent models treat the environment in a homogeneous sense, where range dependent models are capable of handling environmental variations in range. The technique used in this work's model involves using a three-dimensional parabolic equation (3DPE) to simulate the pressure field through a range dependent water column. The 3DPE model as developed does not account for spatial bottom variability, temporal and spatial variability of the surface, or density variability.

Described by Knepp (1983), a multiple phase screen propagation technique is employed, whereby a given volume is divided into a number of thin layers, each being perpendicular to the direction of propagation. The irregularities in each layer are replaced by the geometric optics phase change imparted after propagation through the layer, or the phase screen.

The split-step Fourier algorithm technique has been utilized extensively to solve the PE and is likewise used to solve the 3DPE in this work. Jensen et al. (1994) derives

6

the split-step marching solution in cylindrical coordinates. This work uses a Cartesian coordinate form such that

$$\psi(x, y, z) = F_{k_z, k_y}^{-1} \left\{ e^{-\frac{i\Delta x}{2k_0}(k_z^2 + k_y^2)} F_{z,y} \left\{ e^{\frac{ik_0}{2}[n^2(x_0, y_0, z_0) - 1]\Delta x} \psi(x_0, y_0, z_0) \right\} \right\}, \qquad (11)$$

where a Fourier transform in y and z is applied to the original wave function and phase screen functions, $\psi(x_0, y_0, z_0)$ and $\exp\left\{ \frac{ik_0}{2}[n^2(x_0, y_0, z_0) - 1]\Delta x \right\}$ respectively. The final result is obtained by applying the inverse Fourier transform to the aforementioned calculation and free propagator function $\exp\left\{ -\frac{i\Delta x}{2k_0}(k_z^2 + k_y^2) \right\}$.

The stability of this method concerning a 2DPE model was confirmed for 75, 150 and 300 Hertz by Young (2006). Results from the 3DPE model were then compared to those of the 2D case to ensure accuracy. Due to computational restrictions, this work provides an analysis of 75 and 150 Hz only.

Proper computational parameters for the 3DPE model were then established as seen in Table 1. Of importance were the lateral and depth grid spacings, (dy) and (dz) respectively, and two march-step intervals (dx) and (dxx). If parameter values were too large, the simulated acoustic pressure field lacked accuracy. If too small, computing time and memory constraints became an issue.

Two march-step intervals were used in the 3DPE model to optimize computing time. The first, (dx), was chosen as the base march-step interval and was found to provide accurate results when compared to a similar 2DPE model. The second, (dxx), smaller march-step was established primarily to provide a smaller interval over which energy flux intensities could be evaluated. The smaller march-step was applied once for every base march-step. This considerably decreased computing time as compared to using the smaller march-step exclusively. The computational parameters chosen for the 3DPE model in this work are provided in Table 1.

Base march-step interval	dx		10 m
Small march-step interval	dxx		1 m
Lateral grid spacing	dy		0.73 m
Depth grid spacing	dz		0.73 m
Range	x		5000 m
Lateral extent	y_{max}		3000 m
Maximum computational depth	D		375 m

Table 1.   Grid spacing and march-step interval parameters.

C.   BOUNDARY CONDITIONS

The ocean surface was modeled as a pressure release boundary using an image ocean. This imposed the constraint of zero pressure at the surface $\psi(x, y, 0) = 0$. The bottom and lateral boundary conditions were absorbing in nature. Boundary attenuation was achieved by introducing artificial sponge layers in such a way that all waves were totally absorbed and no reflection occurred. This was accomplished by imposing a gradual loss of amplitude as y approached the lateral limits and z approached the bottom. The form of the loss at each step is

$$L(y,z) = \exp\left\{-\beta dx\left[e^{-\left(\frac{y-y_{max}}{\alpha y_{max}}\right)^2} + e^{-\left(\frac{z-D}{\alpha D}\right)^2}\right]\right\}, \tag{12}$$

where $\alpha = 0.08$, $\beta = 0.04$ and D is the maximum computational depth. This form effectively prevents any acoustic energy from penetrating $\alpha \times D \simeq 8$ m above the bottom and likewise, $\alpha \times y_{max} \simeq 12$ m from the lateral boundaries.

D.   SOURCE/STARTING FIELDS

The 3DPE model uses an analytical source function designed to match the farfield result for a point source solution of the Helmholtz equation in a homogeneous medium.

The result of the derivation of a Gaussian point source found in Jensen et al. (1994) was used in this work:

$$\psi\left(x=0, y=0, z\right) = k_0 e^{-\frac{k_0^2}{2}(z-z_s)^2} , \tag{13}$$

where k_0 is the effective source level and z_s is the source depth. The value of k_0 is obtained by

$$k_0 = \frac{2\pi f_0}{c_0} , \tag{14}$$

where f_0 is the frequency and c_0 is the reference sound speed. In this work, the reference sound speed was 1500 m/s and the source depth 50 m.

E.   EXTRACTION OF MODE AMPLITUDES

Normal mode amplitudes were calculated for modes one through twenty in this work. They were extracted by expanding the function $\psi\left(x, y, z\right)$ in terms of the unperturbed modes, ϕ_n, yielding

$$\psi\left(x, y, z\right) = \sum_{n=1}^{N} A_n\left(x, y\right)\phi_n\left(z\right) \tag{15}$$

and

$$\left(\frac{\partial^2}{\partial z^2} - \bar{k}^2\left(z\right) - k_n^2\right)\phi_n = 0 , \tag{16}$$

where $A_n\left(x, y\right)$ are the mode amplitudes and $\bar{k} = \omega/\bar{c}\left(z\right)$ (Colosi, 2006).

The mode amplitude equation is obtained by substituting equation (15) into the three-dimensional parabolic equation (10), multiplying by the mode function ϕ_m and integrating over depth to yield

$$\frac{\partial \varphi_n}{\partial x} + \frac{i}{2k_0}\frac{\partial^2 \varphi_n}{\partial y^2} = -i\sum_{m=1}^{N}\rho_{mn}\left(x, y\right)e^{il_{mn}x}\varphi_m , \tag{17}$$

where

9

$$\rho_{mn}(x,y) = k_0 \int_{-D}^{0} \frac{\delta c(x,y,z)}{c_0} \phi_n(z)\phi_m(z)\, dz, \tag{18}$$

$$\varphi_n(x,y) = A_n(x,y) e^{-il_n x}, \tag{19}$$

$$l_n = k_n^2/2k_0, \tag{20}$$

$$l_{mn} = l_m - l_n = \frac{k_m^2 - k_n^2}{2k_0}, \tag{21}$$

and D is the computational depth.

Rather than attempt the solution for Equation (17), the mode amplitudes were obtained by solving Equation (10) for the pressure field $\psi(x,y,z)$, and multiplying by the unperturbed modes, ϕ_m, then depth integrated to yield (Colosi, 1996)

$$A_m(x,y) = \int_0^D \psi(x,y,z)\phi_m(z)\, dz. \tag{22}$$

F.   ENERGY FLUX INTENSITY

The energy flux intensity was calculated for modes one through four in this work. Frisk (1994) defines the energy flux intensity as

$$\vec{I} = \frac{i}{4\omega\rho_0}\left[\psi\vec{\nabla}\psi^* - \psi^*\vec{\nabla}\psi\right], \tag{23}$$

where ρ_0 is a reference density. For normal modes the vertical flux is effectively zero, or $I_z = 0$. Thus the only concern is with components in the x and y directions. For notational efficiency it is useful to define

$$\vec{\nabla}_h(x,y) = \frac{\partial}{\partial x}\hat{x} + \frac{\partial}{\partial y}\hat{y}. \tag{24}$$

Expanding equation (23) in terms of the unperturbed modes yields

$$\vec{I} = \frac{i}{4\omega\rho_0}\left[\left(\sum_{n=1}^{N} A_n\phi_n\right)\vec{\nabla}\left(\sum_{m=1}^{N} A_m^*\phi_m\right) - \left(\sum_{m=1}^{N} A_m^*\phi_m\right)\vec{\nabla}\left(\sum_{n=1}^{N} A_n\phi_n\right)\right]. \tag{25}$$

10

Equation (25) now yields

$$\vec{I} = \frac{i}{4\omega\rho_0}\left[\left(\sum_{n=1}^{N} A_n\phi_n\right)\left(\sum_{m=1}^{N}\vec{\nabla}_h A_m^*\phi_m\right) - \left(\sum_{m=1}^{N} A_m^*\phi_m\right)\left(\sum_{n=1}^{N}\vec{\nabla}_h A_n\phi_n\right)\right], \quad (26)$$

which when depth integrated becomes

$$\vec{I} = \frac{i}{4\omega\rho_0}\left[\left(\sum_{n=1}^{N}\sum_{m=1}^{N} A_n\vec{\nabla}_h A_m^*\int_0^D \phi_n\phi_m dz\right) - \left(\sum_{m=1}^{N}\sum_{n=1}^{N} A_m^*\vec{\nabla}_h A_n\int_0^D \phi_m\phi_n dz\right)\right]. \quad (27)$$

Because of mode orthogonality, this results in

$$\vec{I} = \frac{i}{4\omega\rho_0}\left[\left(\sum_n A_n\vec{\nabla}_h A_n^*\right) - \left(\sum_n A_n^*\vec{\nabla}_h A_n\right)\right], \quad (28)$$

leading to the modal energy flux intensity equation used in the 3DPE model:

$$\vec{I}_n(x,y) = \frac{i}{4\omega\rho_0}\left[A_n\vec{\nabla}_h A_n^* - A_n^*\vec{\nabla}_h A_n\right]. \quad (29)$$

Note that the small range step dxx discussed in section B is used to numerically compute the range derivatives $\partial/\partial x$ in Equation (29).

G. SOUND SPEED FIELD

The environment used in this work was a range independent background waveguide consisting of four layers: Surface layer, thermocline, below thermocline isovelocity layer and an isovelocity bottom layer. Transitions between these layers were treated with a hyperbolic tangent. The unperturbed sound speed field was obtained using the following equation:

$$\bar{c}(z) = \left(c_s - \left|\frac{c_s - c_l}{2}\right|\right)\left(1 + \tanh\left[\frac{z - z_{th}}{\Delta_{th}}\right]\right) + \left|\frac{c_l - c_b}{2}\right|\left(1 + \tanh\left[\frac{z - (z_b + 4L)}{L}\right]\right), \quad (30)$$

where c_s is the surface sound speed, c_l the below thermocline sound speed, c_b the bottom sound speed, z_b the bottom depth, z_{th} the central depth of the thermocline, Δ_{th} the thermocline width, and L the transition length scale. The transition length scale

is needed because of the Fourier split-step numerical method. Figure 1 depicts the unperturbed sound speed profile. Table 2 displays the values used in the 3DPE model.

Surface sound speed	c_s	1520 m/s
Below thermocline sound speed	c_l	1480 m/s
Bottom sound speed	c_b	1980 m/s
Bottom depth	z_b	75 m
Central thermocline depth	z_{th}	30 m
Thermocline width	Δ_{th}	15 m
Transition length scale 75 Hz	L_{75Hz}	20 m
Transition length scale 150 Hz	L_{150Hz}	10 m

Table 2.   Sound speed field parameters.

H.   INTERNAL SOLITARY WAVE

Work by Young (2006) has held that using a Gaussian form of a soliton can accurately approximate the hyperbolic-secant-squared form of a soliton which is an exact solution to the Kortweg de Vries wave equation. Following Young (2006) we introduce a single soliton, or ISW to the sound speed field using the Gaussian form

$$\zeta\left(x, y, z; x_0, y_0, \theta\right) = \frac{\zeta_0}{2}\sin\left(\frac{\pi z}{z_b}\right)\left\{1 - \tanh\left[\frac{z - (z_b - L)}{L}\right]\right\}\exp\left[-\frac{\left[(x - x_0)\sin\theta + (y - y_0)\cos\theta\right]^2}{\Delta_{th}^2}\right]$$

(31)

where ζ_0 is the maximum soliton amplitude, z is depth, z_b the bottom depth, L the transition length scale, Δ_{th} the soliton width, θ the angle between the x-axis and ISW,

12

and (x_0, y_0) the hinge point about which the ISW rotated. While the 3DPE method could easily accommodate the proper hyperbolic-secant-squared soliton shape, we used the approximate Gaussian shape so that comparisons could be made to the mode coupling theory in Young (2006). The perturbed sound speed field containing the ISW is then obtained by

$$c\left(x, y, z\right) = \overline{c}\left(z\right) + \frac{\partial c}{\partial z} \zeta\left(x, y, z; x_0, y_0, \theta\right). \tag{32}$$

Figure 2 displays the sound speed field in the *xz*-plane containing a single ISW oriented parallel to the *y*-axis at x = 1000 meters.

I.   MODEL VALIDATION

The 3DPE model was validated in three phases. The first test consisted of using a point source to evaluate the spherical spreading along the *x*-axis. The spherical spreading was found to be satisfactory. The second test consisted of using a point-mode source to evaluate cylindrical spreading and the conservation of mode energy. The cylindrical spreading was found to be adequate and numerical coupling was nonexistent for the homogeneous case. In the third test, the results for an ISW angle of 90° (directly across ISW transmission path) were compared to that of Young's 2D calculations using similar soliton parameters and good agreement was found.

THIS PAGE INTENTIONALLY LEFT BLANK

III. MODEL SIMULATIONS AND DISPLAYS

A. MODEL SIMULATIONS

Twenty separate 3DPE model simulations were completed for each frequency, 75 and 150 Hz. The first 3DPE simulation was completed for an unperturbed environment with no ISW referred to as the homogeneous case. Rotational limiting cases were then defined and simulated. The lower limiting case was defined as the 0° ISW angle at which the ISW was oriented along the x-axis. The upper limiting case was defined as the 90° ISW angle at which the ISW was oriented perpendicular to the x-axis and centered at $x = 1000$ m . Lastly, 3DPE model simulations were completed every 5° between the two limiting cases. Figure 3 displays the ISW locations used in the model simulations.

For each simulation the mode amplitudes $A_n(x, y)$ were computed as well as the energy flux vectors $\vec{I}_n(x, y)$. For the purposes of displaying the change in mode energy for the various cases we formed the ratio $|A_n(x, y, \theta)|^2 / |A_{n0}(x, y)|^2$, where $|A_{n0}(x, y)|^2$ was the mode energy in the homogeneous case. In this analysis we focus on modes 1-4, although mode 4 of the 150 Hz data sets were found to contain very little energy and became unreliable when normalized by the homogeneous energy.

B. MODEL DISPLAYS

The model results in this work are presented by two methods; 5250 m × 3000 m plan view plots, as in Figure 3, displaying the azimuthal dependence of normal mode energy fluctuation patterns (focusing/defocusing) and refractive effects, and waterfall plots that demonstrate the same three-dimensional effect as a function of ISW angle for a given range. In the second method, displays were generated for $|A_n|^2 (\hat{x}, y, \theta_0)$ for $\hat{x} = 2$, 2.5, 3, 3.5, 4, 4.5 and 5 km. All plan view plots denote the position of the ISW with a black line. All plots were standardized to display the same intensity range for $|A_n(x, y, \theta)|^2 / |A_{n0}(x, y)|^2$.

THIS PAGE INTENTIONALLY LEFT BLANK

IV. MODEL ANALYSIS

A. ACOUSTIC SCATTERING PHYSICS FOR LIMITING CASE SIMULATIONS

1. 75 Hz Normal Mode Energy Interactions for ISW Limiting Cases

Figure 4 depicts 75 Hz modal energy patterns for the case in which the ISW is propagating in the *y*-direction so that the crest of the ISW is entirely along the *x*-axis defining the 0° ISW angle limiting case. In this orientation there is no gradient of sound speed in the *x*-direction and the gradient is strongest in the *y*-direction; clearly, this case only allows refraction and mode coupling in the *y*-direction. In these figures a clear negative lensing effect is seen such that along the ISW axis (*x*-axis) there is a significant and widening shadow zone of low intensity. Also, there is a strong dependence on mode number for this diverging lens pattern with the largest change in modal energy seen for mode 2. Figure 5 shows the fractional change in mode energy along the shadow zone axis (*x*-axis) and it is clear that significant mode coupling is occurring, especially between modes 1 and 2 where the mode energy appears to oscillate back and forth between the modes. Also note that the spherical spreading of the mode energies has been taken out of this display because we normalize by $\left| A_{n0} \left(x, y \right) \right|^2$. Thus the decrease in energy with range seen in Figure 5 is due to the negative gradients in sound speed experienced perpendicular to, and on either side of the ISW. The acoustic energy flux, covered in part B of this analysis, indicates refraction angles up to 5° near the ISW. Thus, in this geometry there is a clear combination of scattering mechanisms involving both refraction and mode coupling.

Figure 6 displays the modal energy patterns for the case in which the ISW is propagating in the *x*-direction, so that the crest is entirely parallel to the *y*-axis defining the 90° ISW angle limiting case. In this orientation there is no gradient of sound speed in the *y*-direction and the gradient is strongest in the *x*-direction; clearly this case only allows mode coupling in the *x*-direction. The acoustic energy flux shows a complete absence of refraction in this geometry. Thus, there is no 3D effect exhibited in these figures since the mode energy simply shifts as the acoustic field passes the 1000m range.

Figure 7 shows the fractional change in mode energy along the *x*-axis demonstrating moderate mode coupling, particularly between modes 2 and 3.

2.   150 Hertz Normal Mode Energy Interactions with ISW for Limiting Cases

For the 150 Hz simulations, Figures 8 and 9 show significant initial modal energy in the first three modes, while mode 4 is very weak (see especially Figure 9). In contrast, the first four modes contained significant mode energy in the 75 Hz simulations as seen in Figures 5 and 7. As in the 75 Hz simulations, strong mode coupling exists between the first three modes with gradual energy depletion in all modes along the axis of the ISW in the along ISW transmission path with moderate mode coupling evident between modes two and three after interaction with the ISW in the strictly across-ISW transmission path. Figure 10 shows that the symmetric 3D effect for the 150 Hz case in the along ISW acoustic transmission path is similar to that of the 75 Hz case.

B.   ACOUSTIC ENERGY FLUX

Although three-dimensional effects are observed concerning all modes, they are most dramatic and best expressed by mode 2. Hence, figures representing characteristic behavior are provided for mode 2 exclusively in the remainder of this work.

As the ISW is rotated, two distinct regimes become apparent based on an evaluation of the acoustic energy flux. Figure 11 displays the 75 Hz mode 2 energy fluctuation for an ISW angle of 5°. The boxed regions refer to Figures 12 and 13 which illustrate the acoustic energy flux vectors for both the unperturbed (no ISW) simulation and the perturbed (ISW) case. Figure 12 shows only a change in magnitude between the unperturbed and perturbed acoustic fluxes indicating mode coupling is the only mechanism responsible for focusing modal energy through the ISW. In contrast, Figure 13 displays both magnitude and directional changes in the acoustic fluxes indicating that refraction and perhaps mode coupling are leading to the intense focusing and defocusing along the ISW.

18

Figure 14 displays the energy fluctuation and refraction angles calculated from the differences in acoustic flux between the unperturbed and perturbed simulations for 75 and 150 Hz simulations with a 5° ISW angle. The strongest gradient in sound speed lies near, and is perpendicular with, the ISW. Thus, the extent of the refractive effect is limited to regions near the ISW at range. Further, the highest sound speed is along the crest of the ISW causing negative sound speed gradients on either side of the crest. Thus, the resultant refraction angles are negative in the –y direction from the ISW and positive in the +y direction. Further, refraction of modal energy occurs only for ISW angles of less than 50°. Figure 15 illustrates the last vestige of the refractive effect at an ISW angle of 45° in the 75 Hz simulation, while the refractive effect is negligible concerning the 150 Hz case. This discovery that refraction is important up to a 45° ISW angle is new and much larger than previously predicted (Lynch, Colosi, Gawarkiewicz, Duda, Pierce, Badiey, Katsnelson, Miller, Siegmann, Chiu & Newhall, 2006).

Refraction of mode energy occurs only near the ISW and for lower ISW angles which corresponds to along ISW acoustic transmission paths. The refraction does not appear to be frequency dependent. However, given that only two low frequency simulations were completed a more complete analysis is warranted to justify this statement. Mode coupling appears to occur at all ISW angles corresponding to all acoustic transmission paths, although the coupling is more intense for those paths along the ISW. Further, the mode coupling behavior is frequency dependent.

C. ACOUSTIC SCATTERING PHYSICS FOR ROTATIONAL SIMULATIONS

1. 75 Hz Normal Mode Energy Interactions with ISW for Rotational Cases

Figure 4 depicts strong, symmetric mode energy focusing behavior due to refraction and mode coupling for acoustic transmission paths along the ISW. As the ISW angle increases, the focusing in the refractive regime becomes more intense as seen in Figure 16. The very intense focusing along the source side of the ISW is accompanied by a strong shadow region on the non-source side of the ISW. The upper right panel of

Figure 16 depicts the mode energy fluctuation with a 15$^\text{o}$ ISW angle and is representative of the gradual constriction of the source side focusing region. The lower left panel of Figure 16 displaying the mode energy fluctuation at an ISW angle of 35$^\text{o}$ illustrates the continuing constriction of this focusing region with increasing ISW angle. The along-ISW focusing region becomes virtually nonexistent in response to the decrease in the refractive effect as seen in the lower right panel of Figure 16 displaying the mode energy fluctuation at an ISW angle of 65$^\text{o}$.

Figure 16 also displays regions of alternating focusing and defocusing on the non-source side of the ISW. This effect is caused by mode coupling dependence on the relative phase of modes when they encounter the soliton (Young, 2006).

2. 150 Hertz Normal Mode Energy Interactions with ISW for Rotational Cases

Figures 16 and 17 illustrate the progression of the 3D acoustic energy pattern as the ISW angle increases from 5$^\text{o}$ through 65$^\text{o}$ for 75 and 150 Hz, respectively. Clearly, the energy fluctuation patterns of the 75 and 150 Hz cases are similar; however the effect of the ISW on acoustic energy focusing is stronger at 150 Hz. The magnitude of the focused 150 Hz acoustic energy in the refractive regime along the ISW is 25% higher than that of the 75 Hz case. Further, this frequency dependence is not confined to the refractive regime, but is manifest throughout the simulated waveguide, with the same 25% increase in focused acoustic energy found in the mode coupling regime on the non-source side of the ISW.

3. Energy Focusing/Defocusing as a Function of ISW Angle

To gain insight as to focusing/defocusing of normal mode energy given an acoustic source and ISW angle, it is useful to depict the normal mode energy fluctuation as a function of the ISW angle as explained in Chapter III. Figure 18 illustrates the 75 Hz mode 2 energy fluctuations at ranges of 2.5, 3.5 and 4.5 km.

The greatest effect occurs for ISW angles of less than 20$^\text{o}$. However, there is a marked effect near the ISW for ISW angles up to 45$^\text{o}$ and to a lesser extent for the

remaining ISW angles up to the 90° limiting case. Clearly illustrated is the appreciable effect of the refractive regime for ISW angles of less than 20° noted by the high variability of intensity in the upper left corner of each figure.

Figure 19 displays the 150 Hz mode 2 energy fluctuations at similar range for comparison. The congruency of the pattern and the ISW's effect in the refractive regime are very similar. However, in stark contrast to the 75 Hz case is the increase in intensity within the mode coupling regime seen in the upper right of each figure. While the mode coupling effect was appreciable at 75 Hz at mid-ISW angles (20° to 60°), the effect is much more dramatic at 150 Hz.

THIS PAGE INTENTIONALLY LEFT BLANK

V.   CONCLUSIONS

Although this work considered only a single ISW with varying geometries and two discrete frequencies in one shallow-water acoustic waveguide, important links between the anisotropy imparted by ISWs and the resulting frequency dependent 3D effects have been made. This work has established that two acoustic scattering regimes exist. The refractive regime generates very intense acoustic energy focusing and shadow zones near the ISW but only for geometries where the acoustic transmission path is nearly along the ISW crest (0° to 20°). In contrast, the mode coupling regime produces strong acoustic energy focusing and shadow zones for nearly all geometries, but particularly for along ISW acoustic transmission paths.

Modeling techniques carried out only in separate vertical planes where 3D and mode coupling effects are neglected may be accurate for strictly across ISW propagation paths. However, this work has shown that even a small departure from this geometry results in increased mode coupling and 3D effects. Deterministically, the 3DPE model reveals intensification patterns that are only implied by 2D or $N \times 2D$ methods.

The ISW's effect on the overall 3D acoustic energy pattern was not found to be frequency dependent. However, the ISW's effect on the magnitude of the focusing is frequency dependent. To wit, the 150 Hz simulations display a 25% increase in the magnitude of the focused energy over simulations of the lower 75 Hz frequency. In a relative sense, the effect of this behavior is realized at smaller angular departures from the across-ISW acoustic transmission path for 150 Hz.

Normal mode coupling was shown to go from lower-order modes to higher-order modes and vice-versa. The analysis demonstrates coupling behavior and intensification patterns are governed by the geometry of the acoustic transmission path and ISW. In a practical sense, ISWs focus acoustic energy dependent upon frequency and geometry, which may be exploitable in both a sonar performance and ambient noise modeling sense.

Realistically, 3D intensification and mode coupling effects occur continually as an acoustic field interacts with environmental inhomogeneities. This work has shown the complexity of shallow-water acoustic propagation in the presence of a single ISW.

Future work should explore the stochastic nature of anisotropy within the acoustic waveguide by varying the number, shape and amplitude of ISWs. Further, establishing a realistic acoustic waveguide by including bathymetry and resolving proper surface and bottom attenuation parameters could provide practical results for a comprehensive comparison to observational studies such as the shallow-water acoustic experiment (SW06) off the New Jersey coast in late summer 2006.
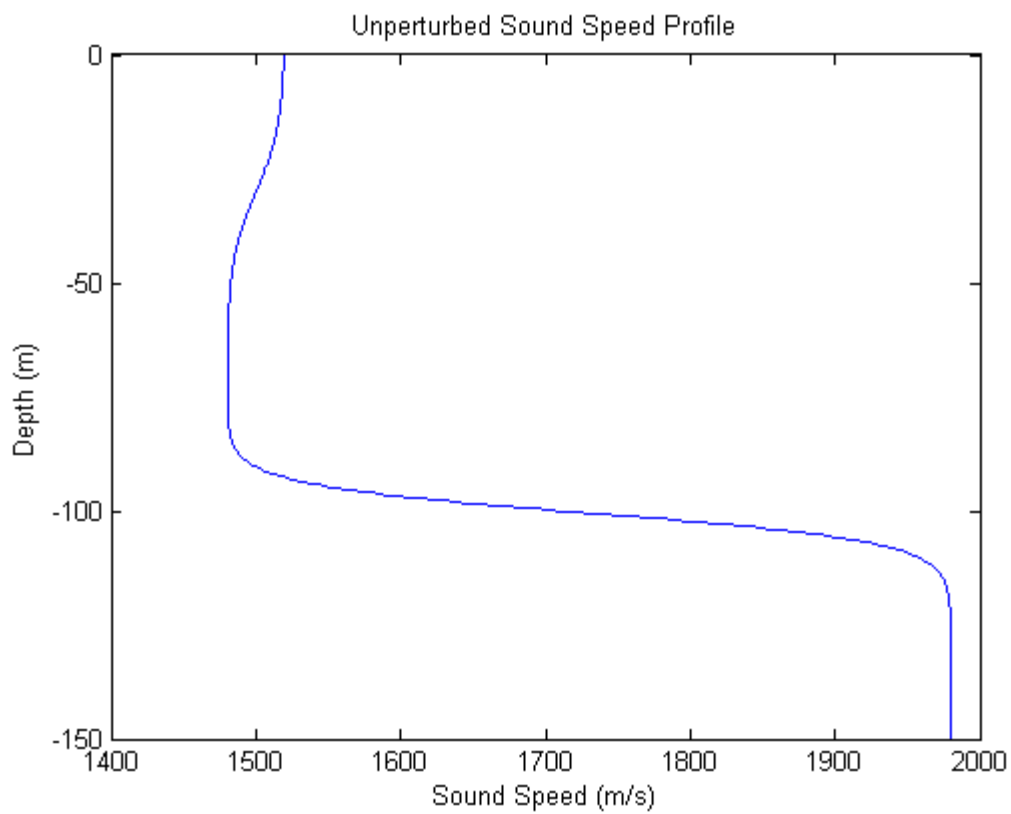
FIGURES

Figure 1.   Background sound speed profile, $\overline{c}(z)$, used in the 3DPE model.
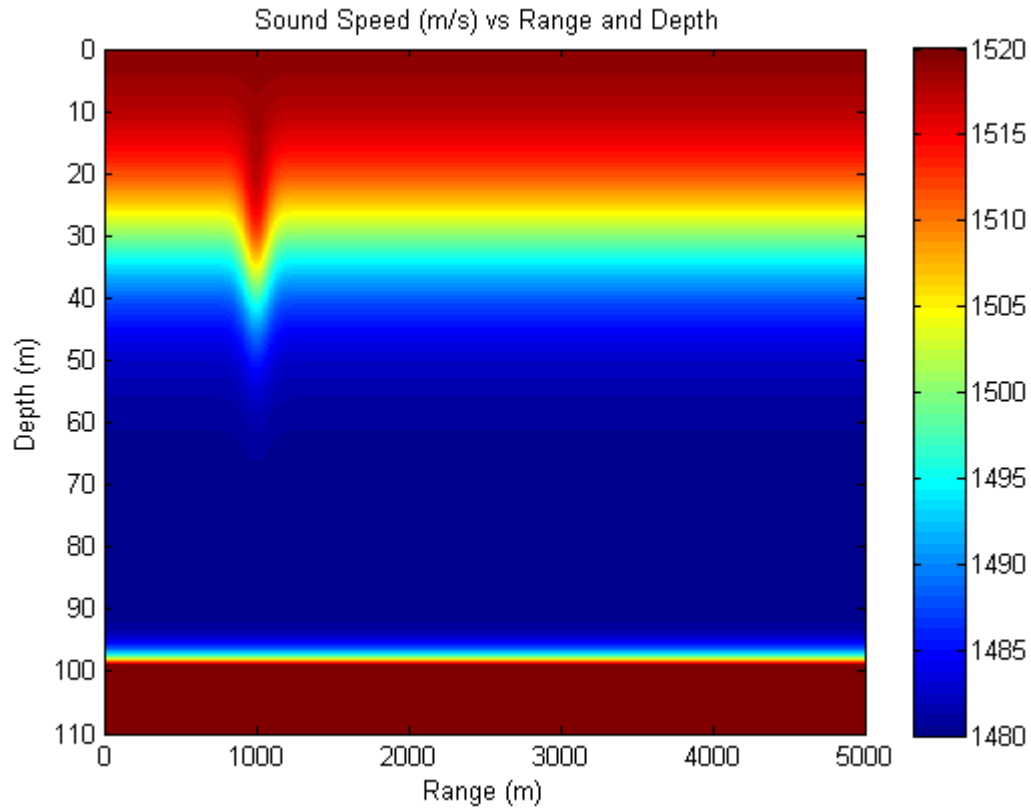
Figure 2.   Perturbed sound speed field in the *xz*-plane centered at *y* = 0. A single ISW is located at *x* = 1000 m with an amplitude of 10 m, width of 100 m, and an angle of 90°.
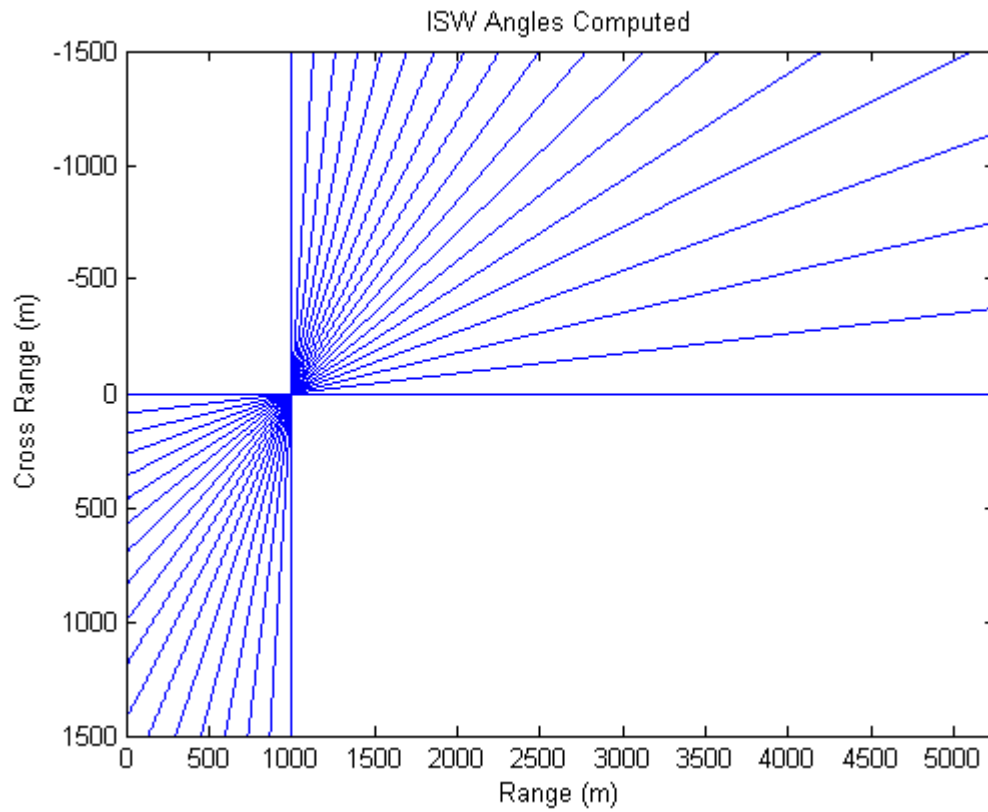
Figure 3.   ISW orientations used in the 3DPE model. Model simulations were completed every five degrees for ISW angles of zero to ninety degrees.
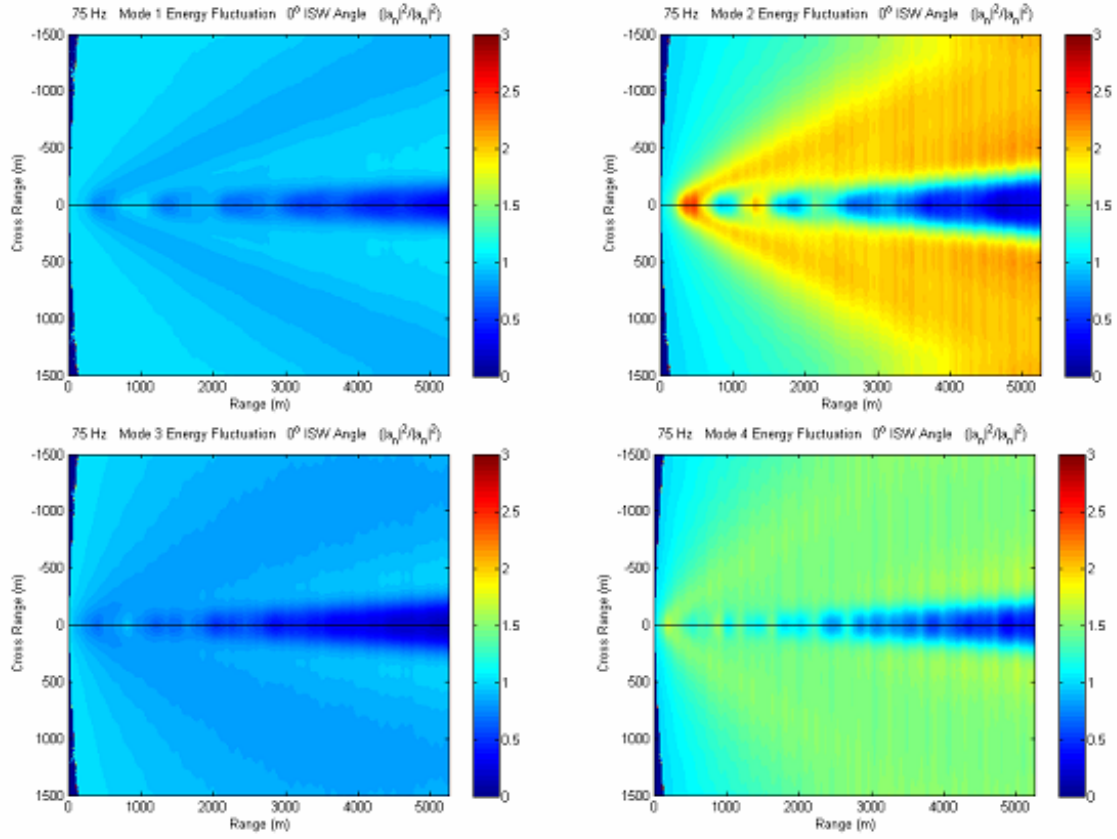
Figure 4. Normal mode energy fluctuation, $|A_n|^2 / |A_{n0}|^2$, at 75 Hz for ISW angle of 0° and modes 1-4. Mode 1 is shown in the upper left panel, mode 2 upper right, mode 3 lower left, and mode 4 lower right.
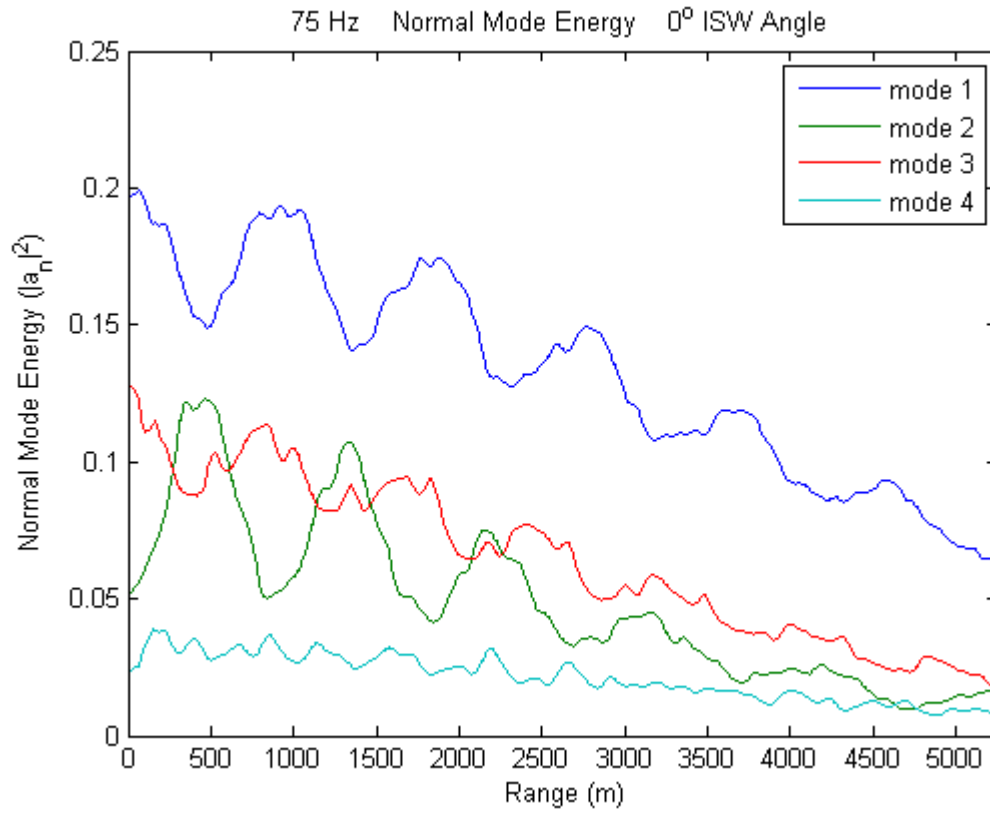
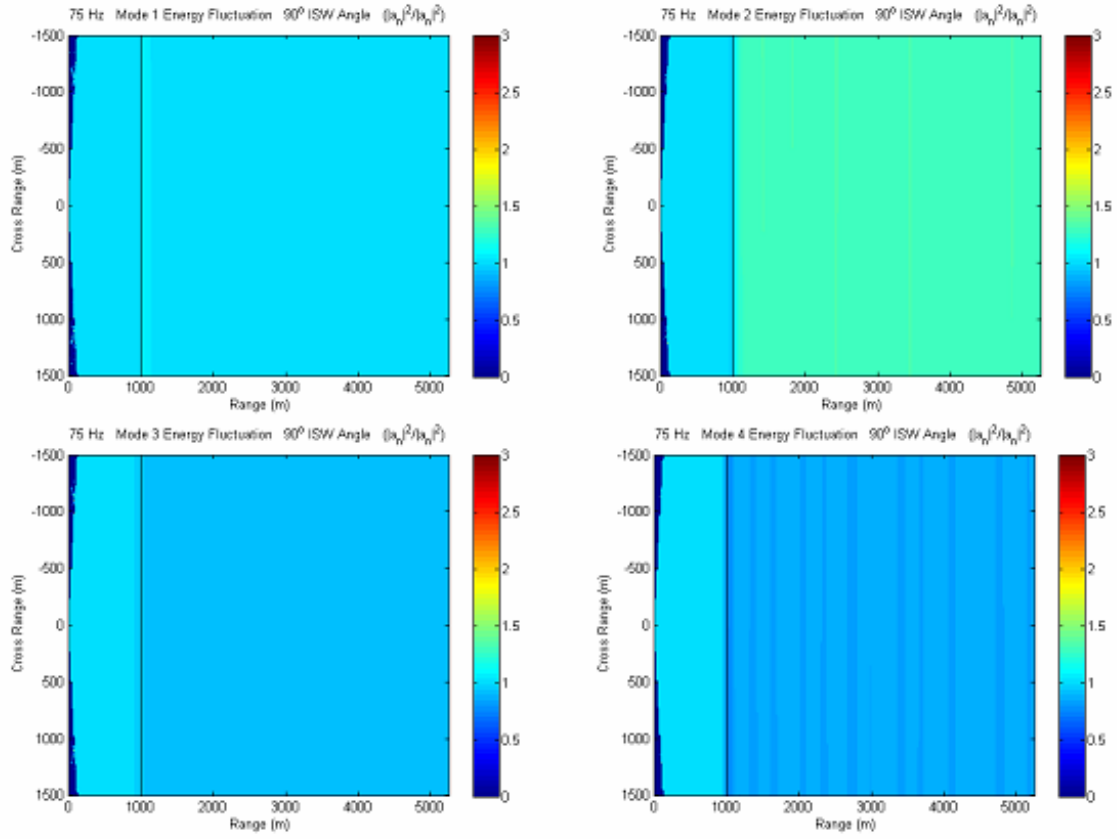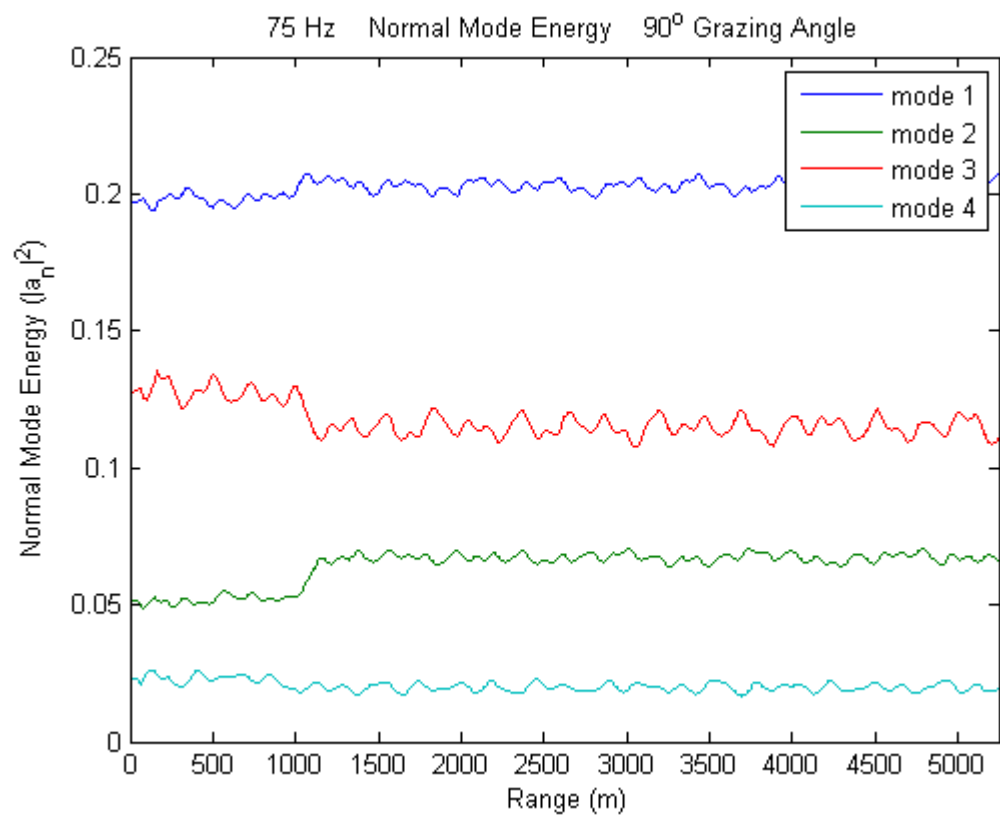Figure 5. Normal mode energy, $|A_n|^2 (x, y = 0)$, at 75 Hz for 0° ISW angle and modes 1-4.
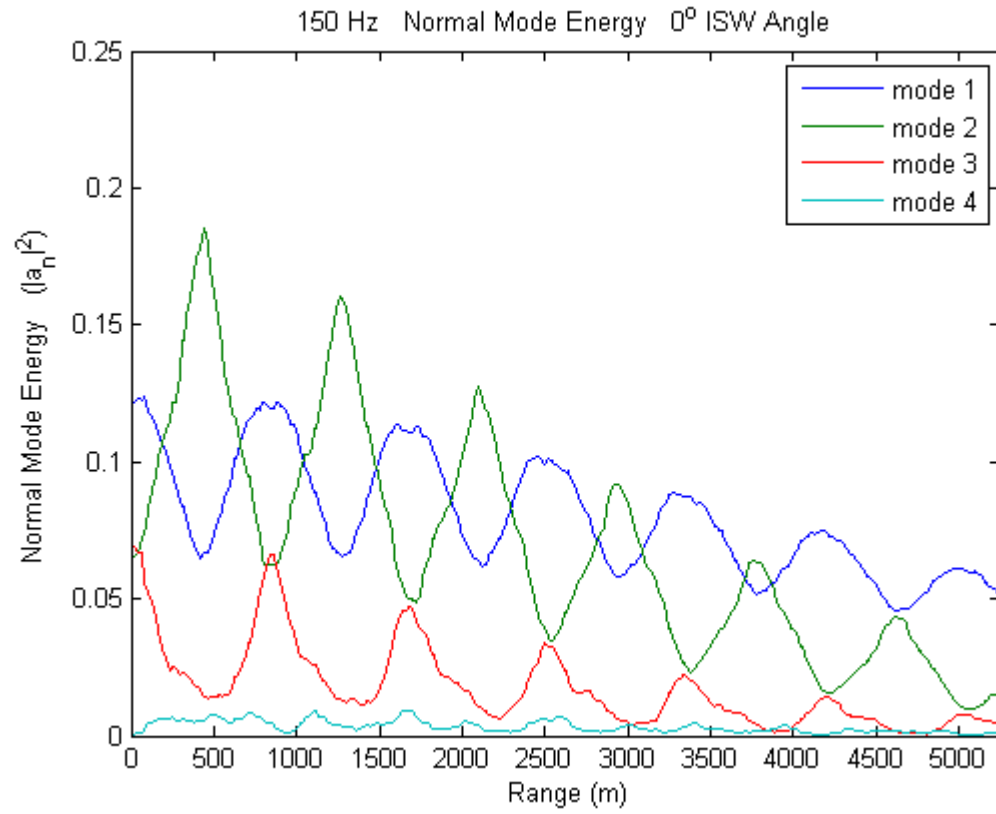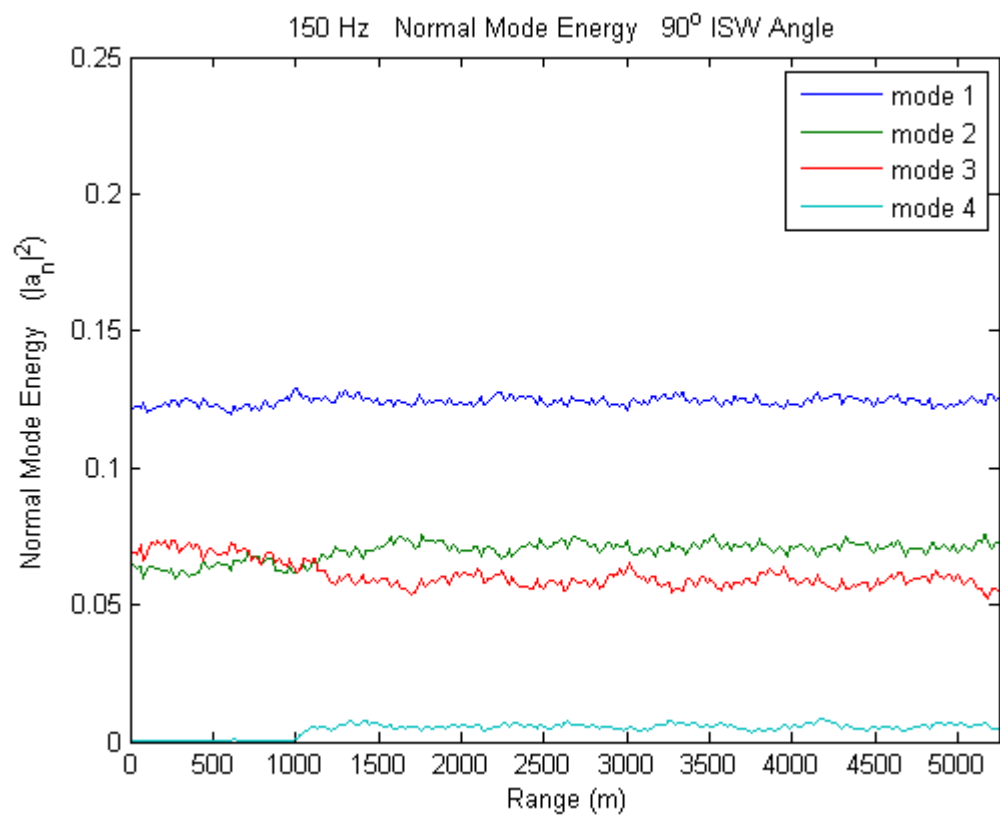
Figure 6. Normal mode energy fluctuation, $|A_n|^2 / |A_{n0}|^2$, at 75 Hz for ISW angle of 90° and modes 1-4. Mode 1 is shown in the upper left panel, mode 2 upper right, mode 3 lower left, and mode 4 lower right.

Figure 7. Normal mode energy, $\left|A_n\right|^2 (x, y = 0)$, at 75 Hz for 90° ISW angle and modes 1-4.

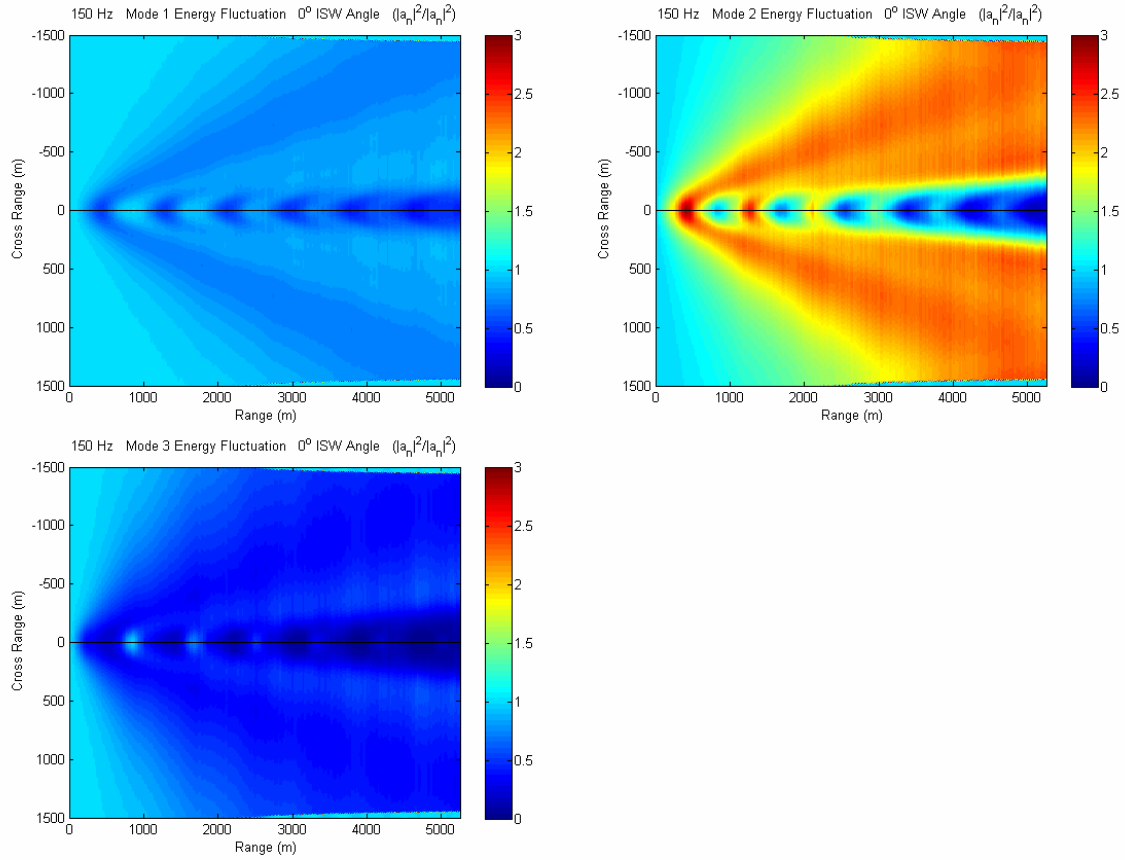Figure 8. Normal mode energy, $|A_n|^2 (x, y = 0)$, at 150 Hz for 0° ISW angle and modes 1-4.

150 Hz   Normal Mode Energy   90° ISW Angle

Figure 9.   Normal mode energy, $\left| A_n \right|^2 \left(x, y = 0 \right)$, at 75 Hz for 90° ISW angle and modes 1-4.

Figure 10.　　　　Normal mode energy fluctuation, $\left|A_n\right|^2 \big/ \left|A_{n0}\right|^2$, at 150 Hz for ISW angle of 0° and modes 1-4. Mode 1 is shown in the upper left panel, mode 2 upper right, and mode 3 lower left.
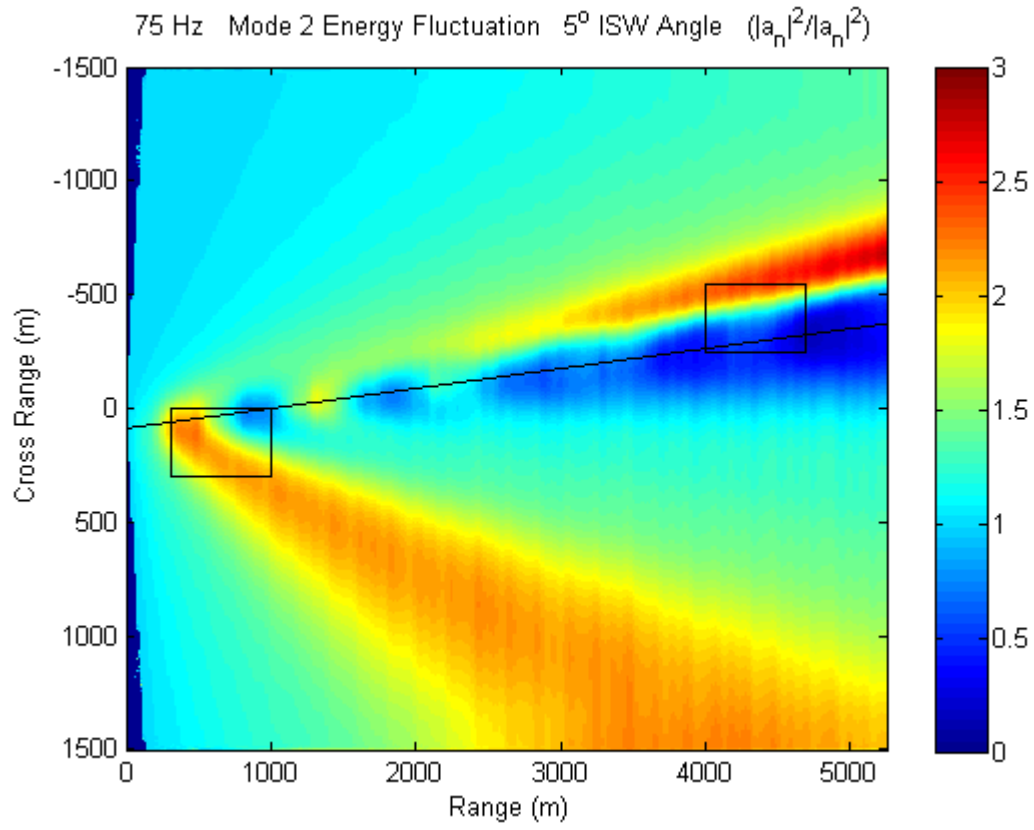
Figure 11.　　　Normal mode energy fluctuation, $\left|A_n\right|^2/\left|A_{n0}\right|^2$, at 75 Hz for ISW angle of 5° and mode 2. The boxed regions correspond to Figures 12 and 13.
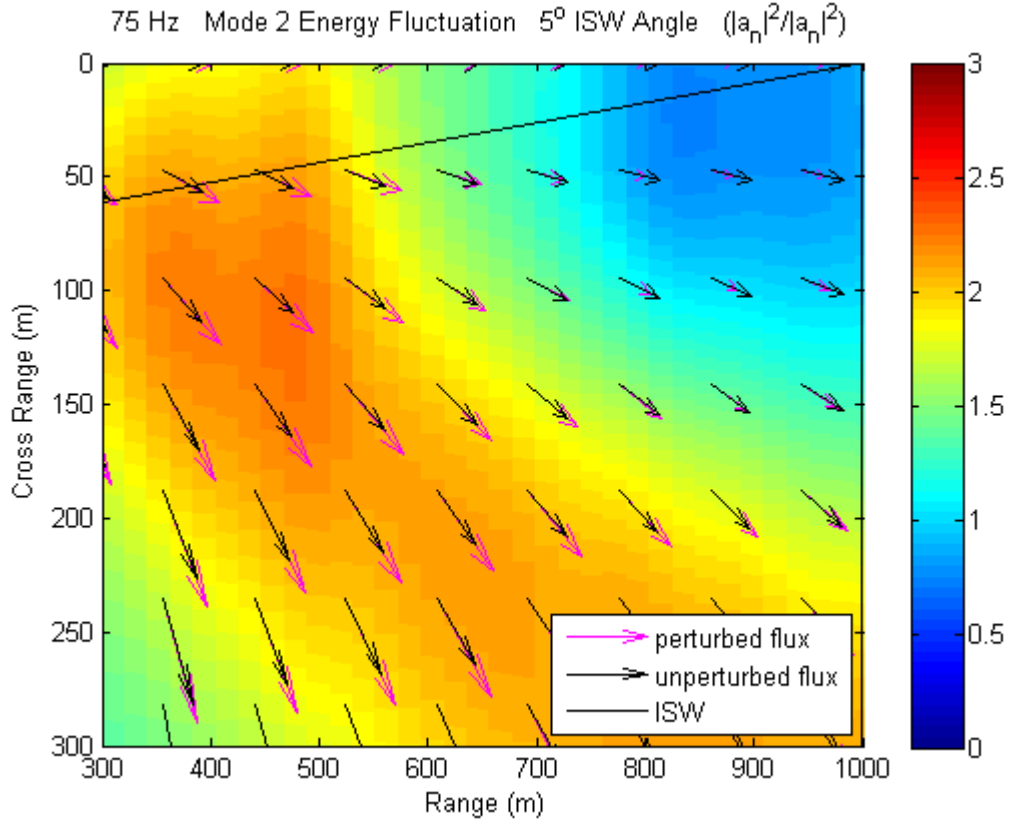
Figure 12. Normal mode energy fluctuation, $\left|A_n\right|^2 \big/ \left|A_{n0}\right|^2$, at 75 Hz for ISW angle of 5° and mode 2, overlaid with the perturbed and unperturbed acoustic energy flux vectors illustrating a mode coupling regime.
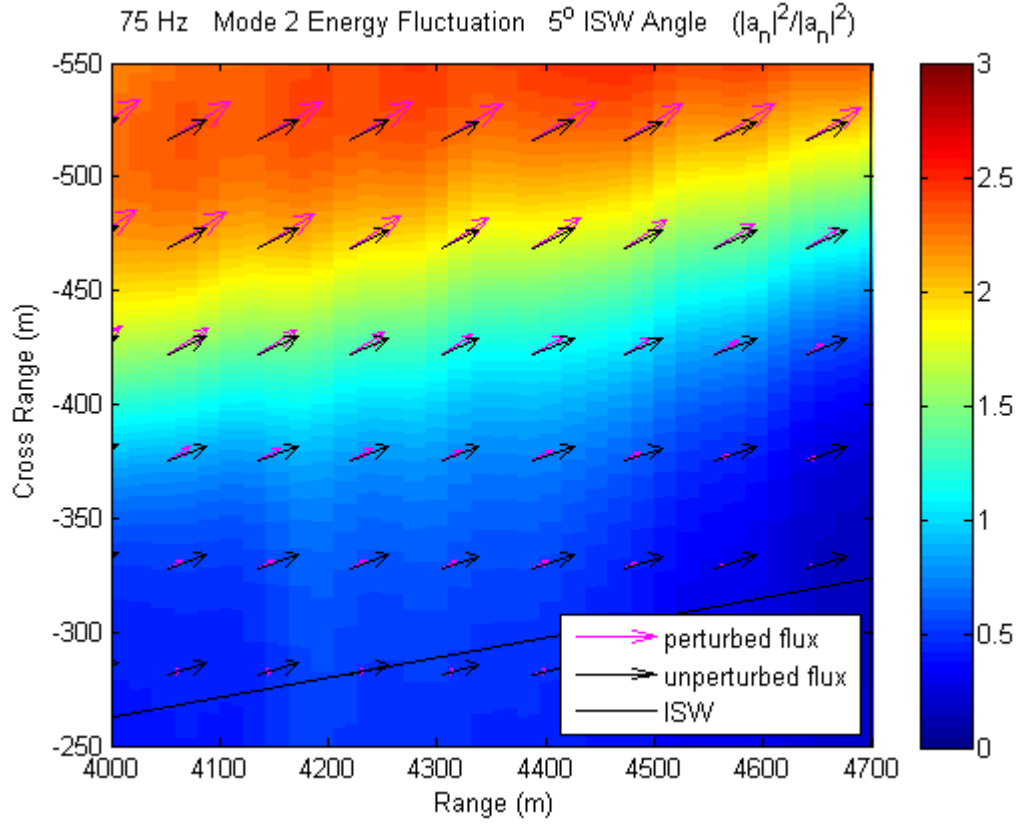
Figure 13. Normal mode energy fluctuation $\left|A_n\right|^2 \big/ \left|A_{n0}\right|^2$, at 75 Hz for ISW angle of 5° and mode 2, overlaid with the perturbed and unperturbed acoustic energy flux vectors illustrating a refractive regime.
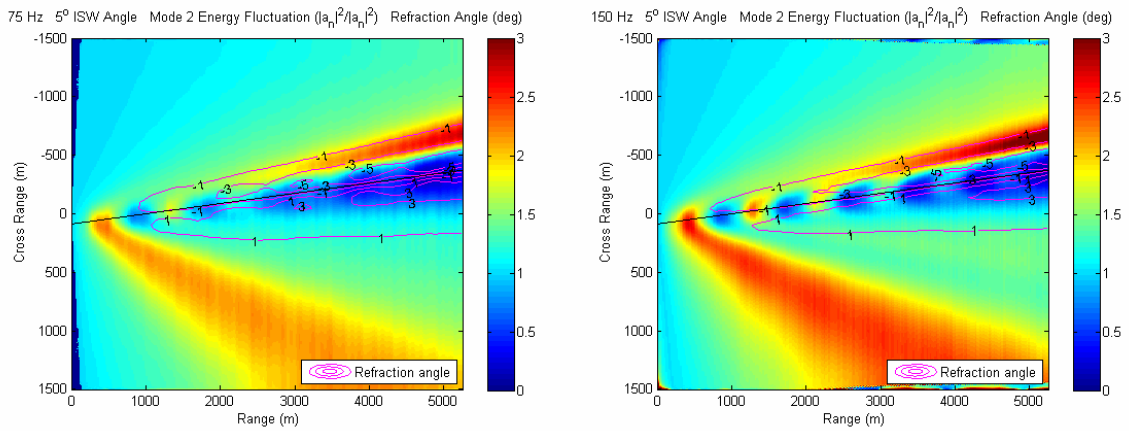

Figure 14. Normal mode energy fluctuation, $\left|A_n\right|^2 \big/ \left|A_{n0}\right|^2$, for ISW angle of 5° and mode 2, overlaid with the refraction angle in degrees. The 75 Hz case is shown in the left panel and 150 Hz on the right.
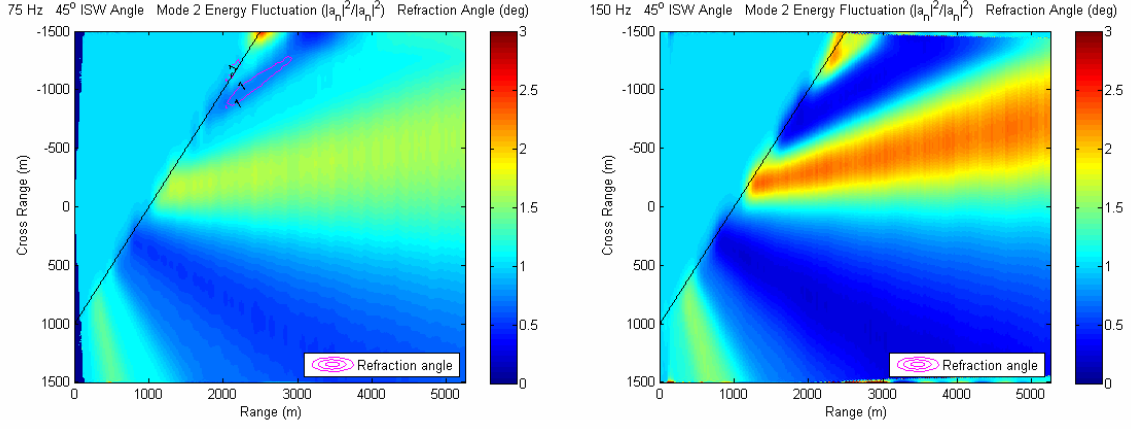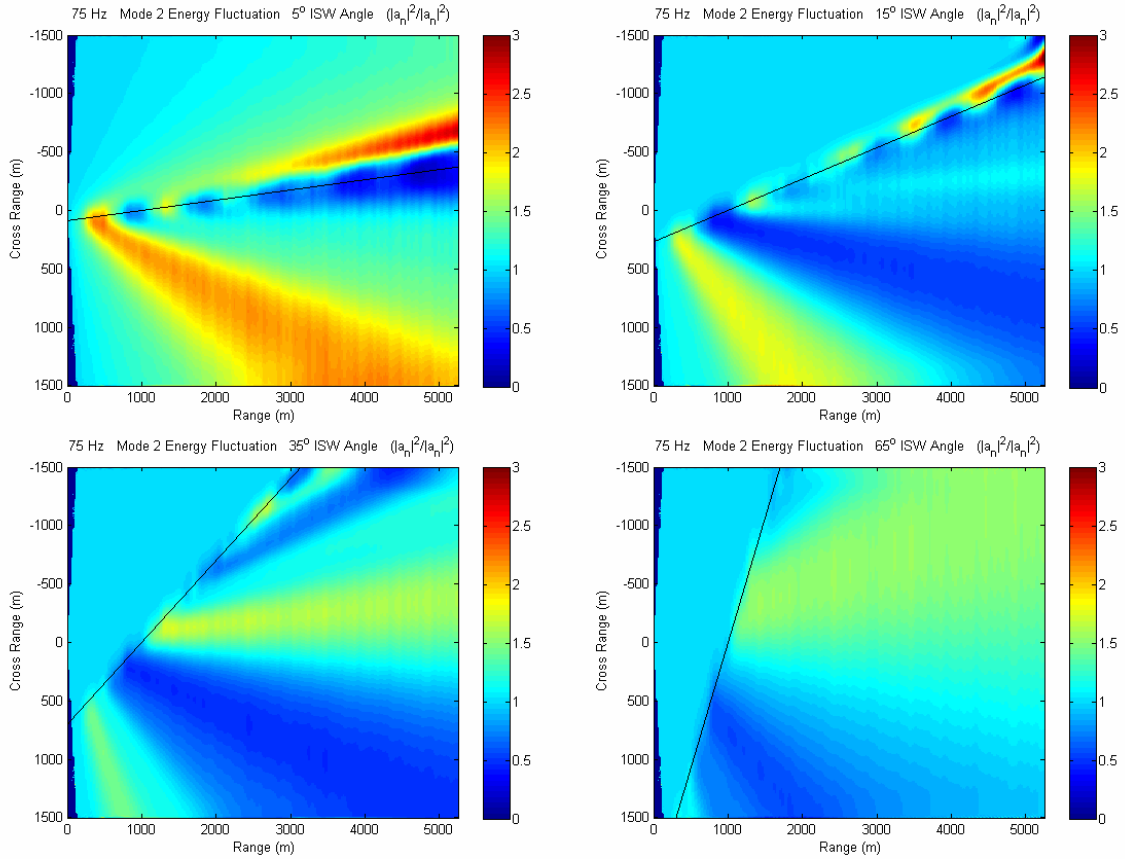
37

Figure 15.　　　　Normal mode energy fluctuation, $\left|A_n\right|^2 \big/ \left|A_{n0}\right|^2$, for ISW angle of 45$^\text{o}$ and mode 2, overlaid with the refraction angle in degrees. The 75 Hz case is shown in the left panel and 150 Hz on the right.

Figure 16.　　　　Normal mode energy fluctuation, $\left|A_n\right|^2 \big/ \left|A_{n0}\right|^2$, at 75 Hz for mode 2 and ISW angles of 5$^\text{o}$, 15$^\text{o}$, 35$^\text{o}$ and 65$^\text{o}$. The fluctuation pattern for the 5$^\text{o}$ ISW angle is shown in the upper left panel, 15$^\text{o}$ upper right, 35$^\text{o}$ lower left, and 65$^\text{o}$ lower right.

Figure 17.   Normal mode energy fluctuation, $\left|A_n\right|^2 \big/ \left|A_{n0}\right|^2$, at 150 Hz for mode 2 and ISW angles of 5°, 15°, 35° and 65°. The fluctuation pattern for the 5° ISW angle is shown in the upper left panel, 15° upper right, 35° lower left, and 65° lower right.
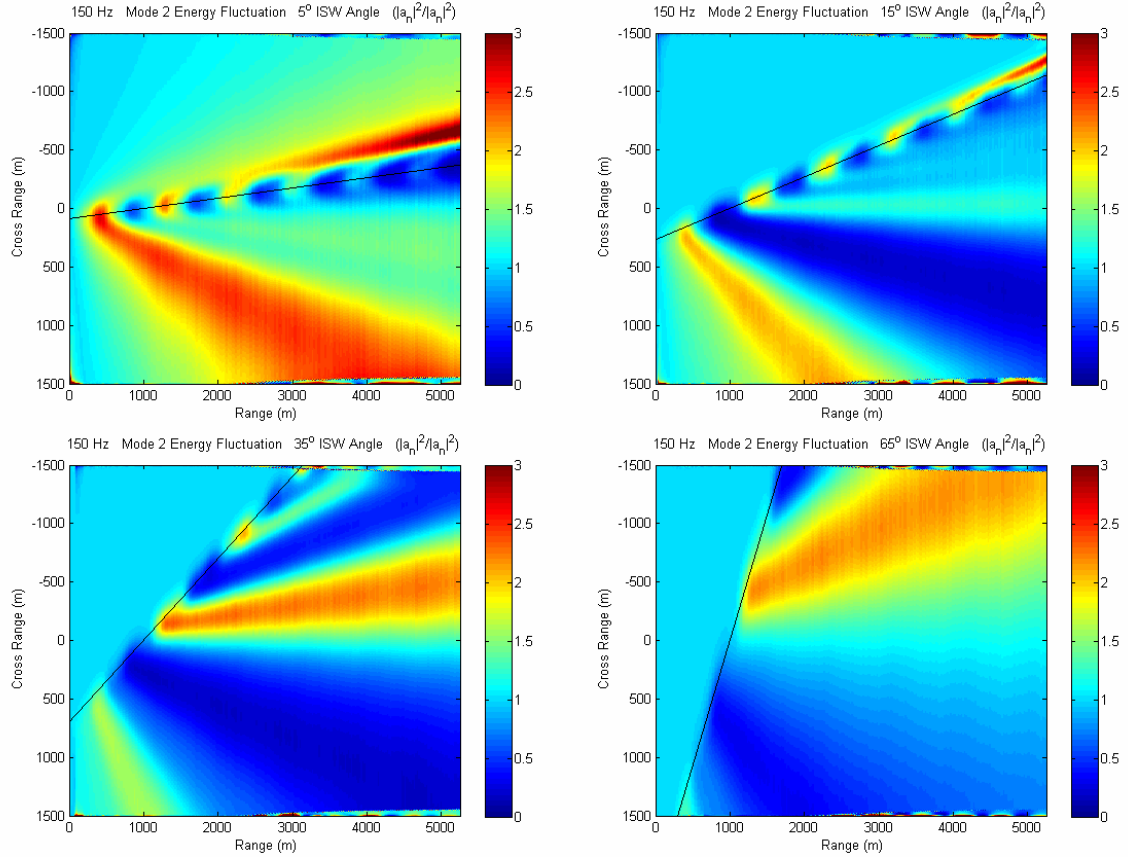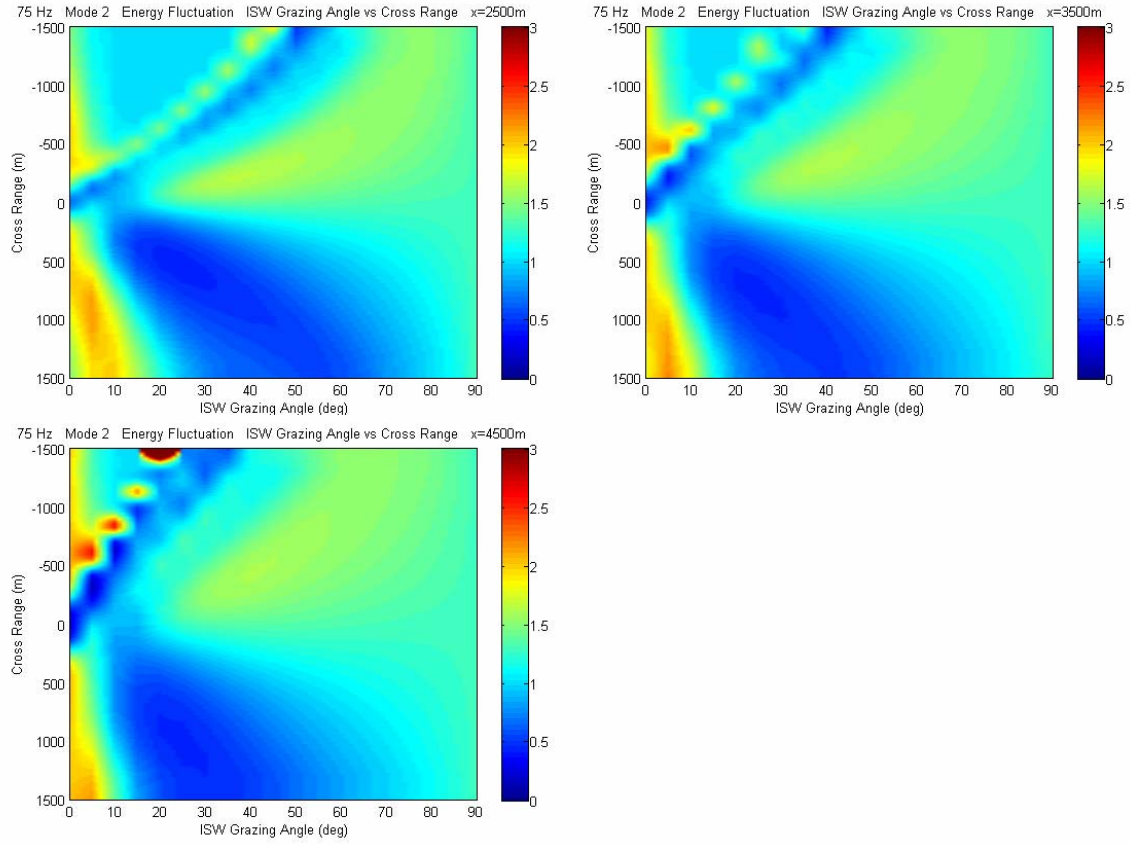
Figure 18.　　　Normal mode energy fluctuation as a function of ISW angle, $\left|A_n\right|^2 \big/ \left|A_{n0}\right|^2$,

at 75 Hz for mode 2 and ranges of 2.5, 3.5, and 4.5 km. The fluctuation pattern for the 2.5 km range is shown in the upper left panel, 3.5 km upper right, and 4.5 km lower left.

Figure 19.　　　Normal mode energy fluctuation as a function of ISW angle, $\left|A_n\right|^2 \big/ \left|A_{n0}\right|^2$, at 150 Hz for mode 2 and ranges of 2.5, 3.5, and 4.5 km. The fluctuation pattern for the 2.5 km range is shown in the upper left panel, 3.5 km upper right, and 4.5 km lower left75 Hz / 65$^\text{o}$ ISW angle / mode 2.
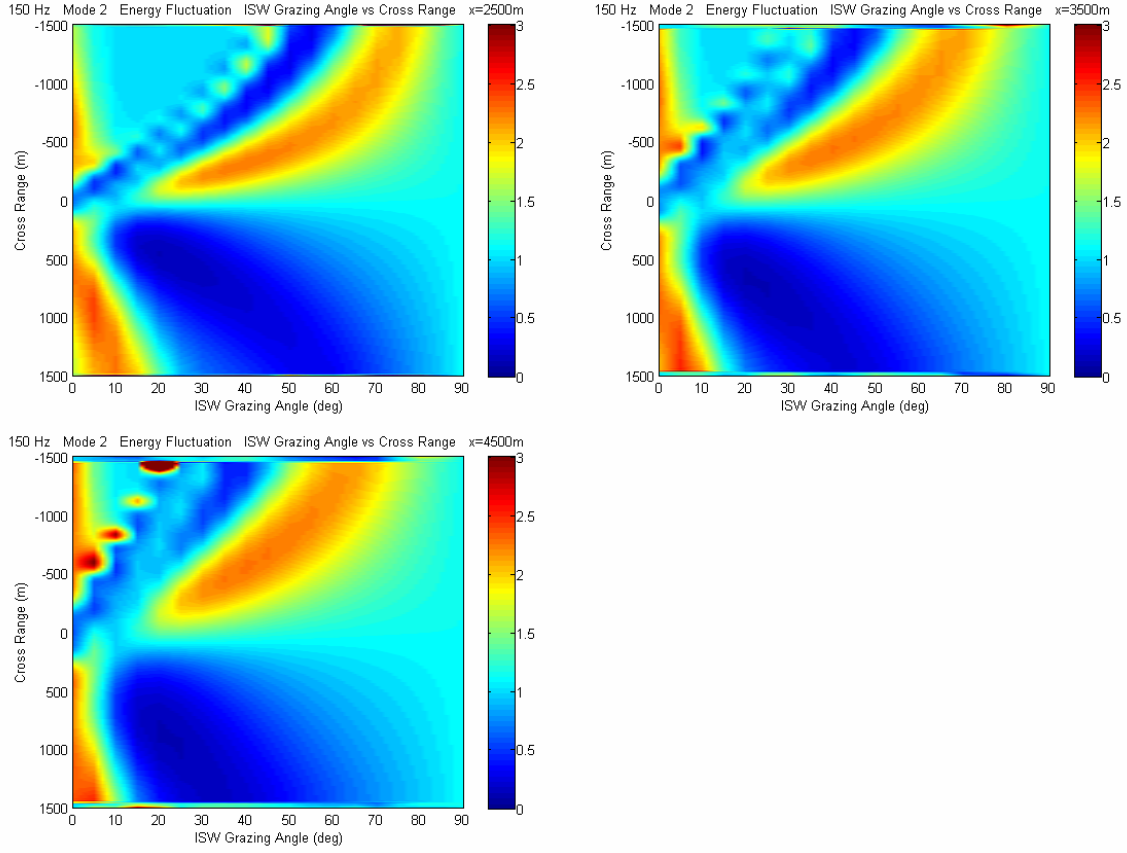
THIS PAGE INTENTIONALLY LEFT BLANK

LIST OF REFERENCES

Colosi, J. A., & Flatte, S. M. (1996). Mode coupling by internal waves for multimegameter acoustic propagation in the ocean. *Journal of the Acoustical Society of America,* 100 (6), 3607-3620.

Colosi, J. A. (2006). Sound through solitons. (Class notes, Naval Postgraduate School, 2006).

Frisk, G. V. (1994). *Ocean and seabed acoustics: A theory of wave propagation.* Upper Saddle River, NJ: P T R Prentice-Hall.

Jackson, C. R. (2004). *An atlas of internal solitary-like waves and their properties* (2nd ed.). Alexandria, VA: Office of Naval Research.

Jensen, F. B., Kuperman, W. A., Porter, M. B., & Schmidt, H. (1994). *Computational ocean acoustics*. Woodbury, NY: American Institute of Physics Press.

Knepp, D. L. (1983). Multiple phase-screen calculation of the temporal behavior of stochastic waves. *Proceedings of the IEEE,* 71 (6), 722-737.

Lynch, J. F., Colosi, J. A., Gawarkiewicz, G., Duda, T. F., Pierce, A. D., Badiey, M., Katsnelson, B., Miller, J. E., Siegmann, W., Chiu, C., & Newhall, A. (2006). Consideration of Finescale Coastal Oceanography and 3-D Acoustics Effects for the ESME Sound Exposure Model. *Submitted to IEEE Journal of Oceanic Engineering Special Issue on the Effects of Sound on the Marine Environment as a Technical Communication.*

Preisig, J. C., & Duda, T. F. (1997). Coupled acoustic mode propagation through continental-shelf internal solitary waves. *IEEE Journal of Oceanic Engineering,* 22 (2), 256-269.

Tielburger, D., Finette, S., & Wolf, S. (1996). Acoustic propagation through an internal wave field in shallow water waveguide. *Journal of the Acoustical Society of America,* 101 (2), 789-808.

Young, A. (2006). Two dimensional acoustic propagation through oceanic internal solitary waves: Weak scattering theory and numerical simulation. (Master's thesis, Naval Postgraduate School, 2006).

THIS PAGE INTENTIONALLY LEFT BLANK

INITIAL DISTRIBUTION LIST

1.   Defense Technical Information Center
        Ft. Belvoir, Virginia

2.   Dudley Knox Library
        Naval Postgraduate School
        Monterey, California

3.   Professor John A. Colosi
        Naval Postgraduate School
        Monterey, California

4.   Professor D. Benjamin Reeder
        Naval Postgraduate School
        Monterey, California

5.   Professor Mary L. Batteen
        Naval Postgraduate School
        Monterey, California

6.   Commander Denise Kruse
        Naval Postgraduate School
        Monterey, California

7.   Robert Creasey
        Naval Postgraduate School
        Monterey, California

THIS PAGE INTENTIONALLY LEFT BLANK